# Advances in Geo-Energy Research

### Original article

## Prediction of proppant accumulation morphology in coal reservoir fractures using numerical simulation and response surface approach methodology

Xuanshi Zhu<sup>1</sup>, Wei Liu<sup>10</sup>\*, Yuanlong Wei<sup>2,30</sup>\*, Peiming Zhou<sup>2,3</sup>, Yifan Wang<sup>4</sup>

#### **Keywords:**

Coalbed methane numerical simulation proppant transport regression analysis model prediction

#### Cited as:

Zhu, X., Liu, W., Wei, Y., Zhou, P., Wang, Y. Prediction of proppant accumulation morphology in coal reservoir fractures using numerical simulation and response surface approach methodology. Advances in Geo-Energy Research, 2025, 18(3): 218-230. https://doi.org/10.46690/ager.2025.12.02

#### **Abstract:**

Proposants are widely employed in coalbed methane extraction. The use of proposant effectively mitigates the closure of hydro-fractures during production, thereby maintaining efficient gas flow pathways. The transport distance and accumulation morphology of proppants within hydro-fractures are critical factors influencing coalbed methane production; however, their quantitative and comprehensive evaluation remains insufficiently explored in coal reservoirs. In this study, a Box-Behnken design was adopted to establish a four-factor, four-level experimental framework for investigating the influence of multiple variables on dune parameters within secondary hydro-fractures through a coupled computational fluid dynamics-discrete element method approach. Response surface methodology and statistical significance testing were employed to quantify the effects of multiple parameters and to establish an empirical predictive model of proppant dune characteristics. The adequacy and significance of the proposed model were verified through analysis of variance. The results demonstrated that both the transport distance and accumulation morphology of proppant within hydro-fractures are jointly controlled by the coupled influence of multiple parameters. Four basic variables, including injection rate, proppant size, proppant density and sand carrying fluid viscosity, were selected, and their influences on sand dune parameters were ranked. The model predictions revealed that dune height may reach up to 79.7% of the hydro-fracture height, while the horizontal dune length can extend up to 15 times the hydro-fracture height. These findings elucidate the mechanisms governing proppant transport and deposition under diverse conditions, offering valuable insights and optimization strategies for proppant selection and injection parameter design in hydraulic fracturing in coalbed methane reservoirs.

#### 1. Introduction

As an important unconventional energy resource, coalbed methane (CBM) is rich in reserves and has great development potential (Xu et al., 2023; Wang et al., 2024). However, to

improve gas recovery from coal reservoirs with extremely low porosity and permeability, it is necessary to adopt stimulation technology (Wu et al., 2023; Eltom, 2024). Hydraulic fracturing has been extensively employed to increase CBM production. In this process, the mixture of sand-carrying fluid

Yandy Scientific Press \*Corresponding author.

E-mail address: zhuxuanshi2022@163.com (X. Zhu); whrsmliuwei@126.com (W. Liu); yuanlongwei1988@126.com (Y. Wei); zpm19900410@163.com (P. Zhou); yifan.wang@geow.uni-heidelberg.de (Y. Wang).

2207-9963 © The Author(s) 2025.

<sup>&</sup>lt;sup>1</sup>State Key Laboratory of Coal Mine Disasters Dynamics and Control, Chongqing University, Chongqing 400044, P. R. China

<sup>&</sup>lt;sup>2</sup>Key Laboratory of Unconventional Natural Gas Evaluation and Development in Complex Tectonic Areas, Ministry of Natural Resources, Guiyang 550009, P. R. China

<sup>&</sup>lt;sup>3</sup>Guizhou Engineering Research Institute of Oil & Gas Exploration and Development, Guiyang 550081, P. R. China

<sup>&</sup>lt;sup>4</sup>Institute of Earth Sciences, Heidelberg University, Heidelberg 69120, Germany

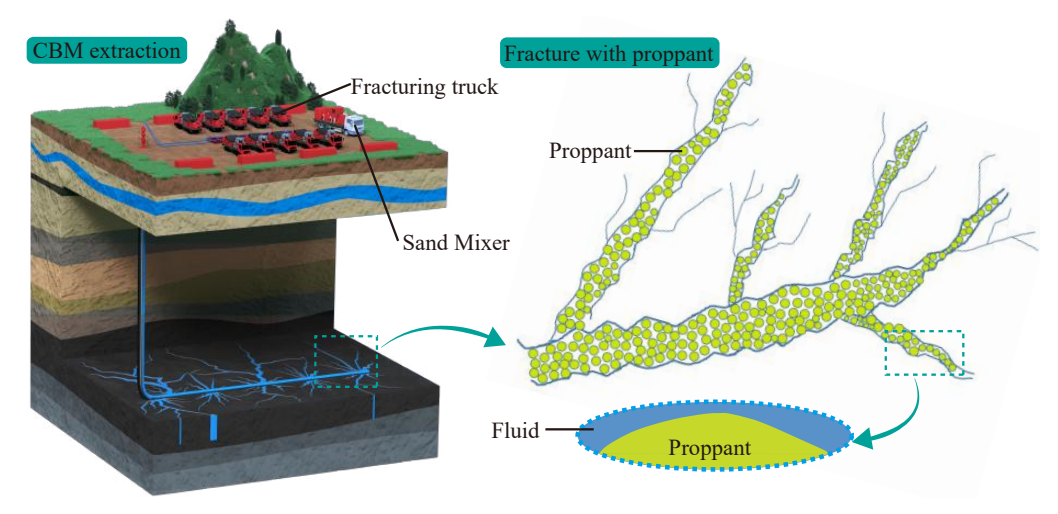


Fig. 1. Proppant in secondary hydro-fractures during CBM extraction.

and proppant is injected into the coal seam through a surface drilled wellbore, forming a complex fracture network, which provides flow pathways for the migration and subsequent production of CBM (Lu et al., 2025; Wei et al., 2025). Compared with sandstone and shale reservoirs, coalbed possesses unique mechanical and structural characteristics, such as low strength, well-developed cleavage systems, obvious heterogeneity, low elastic modulus, and high Poisson's ratio, which make it highly prone to forming numerous secondary fractures during fracturing operations (Mou et al., 2021; Liao et al., 2024). These secondary hydro-fractures occur between coal pores and main hydraulic fractures, acting as essential conduits for CBM flow and thereby playing a crucial role in CBM extraction (Heriawan and Koike, 2015) (Fig. 1). Therefore, it is essential to investigate the distribution patterns of proppant within secondary fractures for elucidating the mechanisms of hydraulic fracturing to increase production in coal reservoirs.

Owing to the lack of effective monitoring techniques, the direct observation of proppant transport distance and accumulation morphology remains a significant challenge (Hou et al., 2022). As such, this issue has been primarily investigated through physical experiments and numerical simulations. The earliest physical investigation of proppant transport was conducted by Kern et al. (1959), who described the settling behavior of proppant between two plexiglass plates. Building upon this foundational work, subsequent studies explored proppant settling in fractures under various conditions, such as outlet configuration effects (Basiuk et al., 2022); transport mechanisms in inclined and horizontal fractures using slick-water experiments (Yamashiro and Tomac, 2022); and proppant transport and distribution within complex fracture networks, revealing that smaller particles can penetrate more deeply (Xiao et al., 2021). In addition, several researchers have investigated the accumulation behavior of proppants in curved fractures (Li et al., 2024); tracked particle trajectories and quantified slurry velocities via image analysis (Ma et al., 2022); and analyzed proppant transport and settling in complex hydro-fractures, revealing distinct deposition patterns compared with conventional fractures (Wen et al., 2016).

Collectively, these studies provide valuable insights into the mechanisms of proppant transportation and deposition control, thus laying a solid foundation for quantitative analyses and advanced numerical simulations of proppant behaviors in hydrofracture network. However, physical simulation experiments are resource demanding and often affected by random factors.

With the rapid development of computing technology, numerical simulation methods have been widely used because they can describe the flow evolution in detail and clarify the internal mechanisms of solid-liquid interactions that are difficult to capture in experiments (Hosseini and Khoei, 2020; Rivas and Gracie, 2020; Patel et al., 2024). At present, the most prevalent approaches for simulating proppant transport are the Eulerian-Lagrangian and Eulerian-Eulerian methods (EEM) (Shiozawa and McClure, 2016; Alvandifar et al., 2025). The EEM treats both the fluid and solid phases as interpenetrating continua, with the two-fluid model being one of the most frequently adopted frameworks. However, this approach cannot fully account for particle-particle and particle-wall interactions (Zhou et al., 2010; Anjum et al., 2025). In contrast, the Eulerian-Lagrangian regards the fluid as a continuous phase and the solid particles as a discrete phase. Within this framework, the computational fluid dynamics-discrete element method (CFD-DEM) has been widely applied, wherein Newton's second law governs the motion of individual particles while fluid flow is described by the Navier-Stokes equations, thereby enabling precise tracking of particle trajectories (Akhshik and Rajabi, 2022; Wood, 2023). Collectively, these numerical approaches offer a robust framework for elucidating the complex coupling between fluid dynamics and particle motion, enabling the realistic simulation of proppant settling behavior.

Building on the above widely used strategies for simulating proppant transport, researchers have analyzed: (1) Corner effects under different fracture-network intersections using the EEM, showing that the turning-angle influence concentrates at corners and persists up to four fracture widths downstream (Cheng et al., 2021); (2) fracture-aperture contrasts, branch-orientation, and tip leak-off using CFD-DEM to quantify their

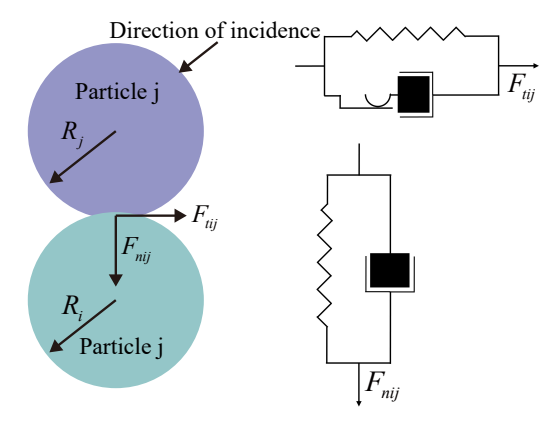


Fig. 2. Schematic of the Hertz-Mindlin model.

impacts on network-scale distribution (Wang et al., 2019; Zheng et al., 2024); (3) coupled pulsed-hydraulic-fracturing and CFD-DEM simulations revealing superior fracture propagation and placement under square-pulsed injection (Li et al., 2023); (4) the influences of various factors on proppant backflow using an improved CFD-DEM approach (Lv et al., 2025); and (5) the role of joint roughness was investigated using a CFD-DEM approach, where increased roughness intensifies proppant-proppant and proppant-wall interactions, thereby enhancing horizontal transport velocity (Suri et al., 2019; Suri et al., 2020). The aforementioned studies provide critical insights into the factors influencing proppant transportation. Especially, the injection rate, proppant size, viscosity of sand-carrying fluid, and proppant density have been identified as the main parameters that control the morphology of proppant dune. However, most previous researches have been limited to the qualitative exploration of relationships between individual parameters and dune characteristics, while research on the coupling effects of multiple variables or the systematic evaluations of their relative importance have been limited. Furthermore, empirical models and quantitative assessments elucidating the variations of dune parameters with respect to proppant properties and injection conditions remain scarce.

In this study, a coupled CFD-DEM proppant transport model was developed, and a Box-Behnken experimental design was implemented to quantitatively investigate the influences of multiple variables on proppant dune parameters in the secondary hydro-fractures. The selected variables include injection rate  $(x_1)$ , proppant size  $(x_2)$ , sand-carrying fluid viscosity  $(x_3)$ , and proppant density  $(x_4)$ . Maximum dune height  $(H_{ma})$ , windward slope angle  $(A_{ws})$ , and leeward slope angle  $(A_{ls})$  were selected as the indexes of proppant placement morphology. In addition, the horizontal distance from the highest point of the dune to the entrances  $(L_{ma})$ was used as an indicator of transport distance. The regression model of sand dune parameters was established by response surface methodology, and the relative significance of each influencing factors was evaluated. Then, the sufficiency and accuracy of the regression models were verified through analysis of variance (ANOVA). The validated models were further used to predict the proppant dune height and horizontal range of proppant dunes under different operating conditions. By combining numerical simulation with response surface methodology, this study establishes an efficient and reliable framework for predicting proppant accumulation morphology in coal reservoirs and offers theoretical guidance for optimizing fracturing parameters in CBM development.

#### 2. Methods

#### 2.1 CFD-DEM model and simulation parameters

#### 2.1.1 Governing equations

During proppant transport, the flow of the sand-carrying fluid is governed by the Navier-Stokes (N-S) equations (Zhu et al., 2008; Shamshirband et al., 2015):

$$\frac{\partial}{\partial t} \left( \varepsilon_f \rho_f \right) + \nabla \cdot \left( \varepsilon_f \rho_f u_f \right) = 0 \tag{1}$$

$$\frac{\partial}{\partial t} \left( \varepsilon_f \rho_f u_f \right) + \nabla \cdot \left( \varepsilon_f \rho_f u_f u_f \right) 
= -\varepsilon_f \nabla p + \nabla \cdot \left( \varepsilon_f \tau_f \right) + \tau_f \rho_f g - F_{fp}$$
(2)

where  $\varepsilon_f$  denotes the fluid volume fraction;  $\rho_f$  represents the fluid density;  $u_f$  denotes the fluid velocity; p represents the pressure; g represents the gravitational acceleration;  $\tau_f$  represents the fluid viscous stress tensor;  $F_{fp}$  represents the momentum exchange term; and t represents time.

The contact forces of particles were calculated by using the Hertz-Mindlin contact model (Richesson and Sahimi, 2019), as shown in Fig. 2. The force between spheres i and j can be expressed as:

$$F_{ij} = F_{nij} + F_{tij} \tag{3}$$

where  $F_{ij}$  represents the collision force;  $F_{nij}$  represents the normal force; and  $F_{tij}$  represents the tangential force between two particles.

The migration of proppant particles follows Newton's second law (Cundall and Strack, 1979), and the balance of governing force is expressed as:

$$F_{fp} = \frac{1}{\Delta V} \sum_{i=1}^{n_p} \left( F_{d,i} + F_{s,i} + F_{m,i} \right) \tag{4}$$

where  $n_p$  is the particle number;  $\Delta V$  denotes the volume of the fluid element; and  $F_{d,i}$ ,  $F_{s,i}$  and  $F_{m,i}$  represent the drag force, Saffman force and Magnus force, respectively.

The total particle-fluid interaction force on sphere i can be expressed as (Cundall and Strack, 1979):

$$f_{pf} = f_d + f_{\nabla p} + f_{\nabla \tau} + f_{um} + f_B + f_s + f_m \tag{5}$$

where  $f_d$  represents the drag force;  $f_{\nabla p}$  represents the pressure gradient force;  $f_{\nabla \tau}$  represents the viscous force;  $f_{um}$  represents virtual mass force;  $f_B$  represents Basset force;  $f_s$  represents lift forces; and  $f_{Mm}$  represents Magnus force.

The drag force was calculated by the Schiller and Naumann drag models (Difelice, 1994):

$$f_d = \frac{1}{8} \rho_f C_d \pi d^2 \varepsilon_f^{2-\zeta} \left( u_f - u_s \right) \left| u_f - u_s \right| \tag{6}$$

where d represents the particle diameter;  $u_f - u_s$  represents the relative velocity, and they can be expressed as (Difelice, 1994):

Table 1. Experimental parameters of proppant transport.

Parameters	Numerical simulation parameters	Comparison test parameter	
Model height (cm)	4.5	90	
Model length (cm)	45	270	
Model width (cm)	0.14	0.14	
Proppant diameter (mm)	0.2~0.5	0.2~0.5	
Proppant Poisson's ratio (-)	0.45	0.45	
Proppant Young's modulus (Pa)	$5 \times 10^6$	$5\times10^6$	
Proppant density (kg/m <sup>3</sup> )	1,500~3,000	1,500~3,000	
Injection rate (L/s)	0.005, 0.006, 0.008, 0.009, 0.010, 0.011, 0.012	1.67	
Sand-carrying fluid density (kg/m <sup>3</sup> )	1,000	1,000	
Sand-carrying fluid viscosity (mPa·s)	1.25~3.5	1	
Wall density (kg/m <sup>3</sup> )	1,200	1,200	
Wall Poisson's ratio (-)	0.37	0.37	
Wall Young's modulus (Pa)	$4.8\times10^9$	$4.8\times10^9$	
Coefficient of static friction*	0.61	0.61	
Tangential coefficients of restitution*	0.5	0.5	
Normal coefficients of restitution*	0.5	0.5	
Coefficient of static friction**	0.5	0.5	
Tangential coefficients of restitution**	0.2	0.2	
Normal coefficients of restitution**	0.2	0.2	
DEM time step (s)	$5.0 \times 10^{-4}$	$5.0\times10^{-4}$	
CFD time step (s)	$5.0 \times 10^{-5}$	$5.0\times10^{-5}$	
Coupling time step (s)	$5.0 \times 10^{-4}$	$5.0\times10^{-4}$	

Notes: \* particle-particle, \*\* particle-wall.

$$C_{d} = \begin{cases} \frac{24}{\text{Re}_{p}}, & \text{Re}_{p} \leq 1\\ \left(0.63 + \frac{4.8}{\sqrt{\text{Re}_{p}}}\right)^{2}, & \text{Re}_{p} > 1 \end{cases}$$

$$\zeta = 3.7 - 0.65 \exp\left[-0.5 \times (1.5 - \log \text{Re}_{p})^{2}\right]$$
 (8)

$$Re_p = \frac{\rho_f d \left| u_f - u_s \right|}{\mu_f} \tag{9}$$

where  $Re_p$  represents the Reynolds number;  $\mu_f$  represents the dynamic viscosity and  $\zeta$  represents the correction factor.

The Magnus force due to particle rotation can be expressed as (Kray et al., 2014):

$$f_{Mag} = \frac{\pi}{8} C_l \pi \rho_f d^3 \left[ \omega \times \left( u_f - u_s \right) \right] \tag{10}$$

where  $C_l$  represents the empirical coefficient (Mei, 1992), and  $\omega$  represents the angular velocity of the particle.

The migration of particle within a narrow channel is influenced by lift forces generated by velocity gradients near the wall of the fluid (Mohapatra and Soares, 2024):

$$f_{saff} = 1.61d^2 \sqrt{\frac{\mu_f}{|\omega_f|}} \left[ \left( u_f - u_s \right) \times \omega_f \right]$$
 (11)

where  $\omega_f$  is the vorticity of the fluid.

#### 2.1.2 Parameter setting

The calculation region was discretized into polyhedral elements, resolving the flow field through a polyhedral mesh. To ensure numerical accuracy, mesh refinement was implemented in narrow regions, maintaining an element size approximately three to five times of the particle diameter. The final mesh consisted of 60,545 units. The shear-stress-transport turbulence model was adopted to simulate turbulent flow (Gislason et al., 2009; Mirjalily, 2023; Li et al., 2025). Transient simulations were performed by using a pressure-based solver combined with gravitational effects, so that the time evolution of proppant transportation could be accurately analyzed. According to Li et al. (2020), the average length, height and aperture of secondary fractures in coal reservoirs formed by hydraulic fracturing were approximately 22.5 m, 2.25 m and 1.4 mm, respectively. In the process of modeling, to reduce calculation cost and facilitate the observation of proppant transportation, the length and height of the fracture were scaled down by a factor of 50. The final model measured 450 mm in length, 45 mm in height and 1.4 mm in aperture. The calculation region consisted of an inlet and an outlet. The inlet face contained five circular ports, each with a diameter of 1.4 mm and a center-to-center spacing of 8.5 mm. A mass-flowinlet boundary condition was imposed to define the injection rate, whereas the proppant mass-flow rate was adjusted to achieve the target sand ratio. At the outlet, a pressure-outlet boundary condition corresponding to atmospheric pressure was imposed. All remaining boundaries were defined as no-slip walls with a roughness height of 1 mm. The time step of fluidparticle coupling was set to  $5.0 \times 10^{-4}$  s, consistent with the time step of the fluid solver. The discrete-element (particle) time step was  $5.0 \times 10^{-5}$  s, the particle-wall static friction coefficient was 0.5, and the normal and tangential restitution coefficients were 0.3, as shown in Table 1. Before injection, the calculation domain was completely saturated with fluid, and then the proppant-fluid mixture was injected through the inlet ports. The solid-liquid two-phase flow simulations were carried out by using ANSYS Fluent 2020 R1 combined with EDEM software 2021.

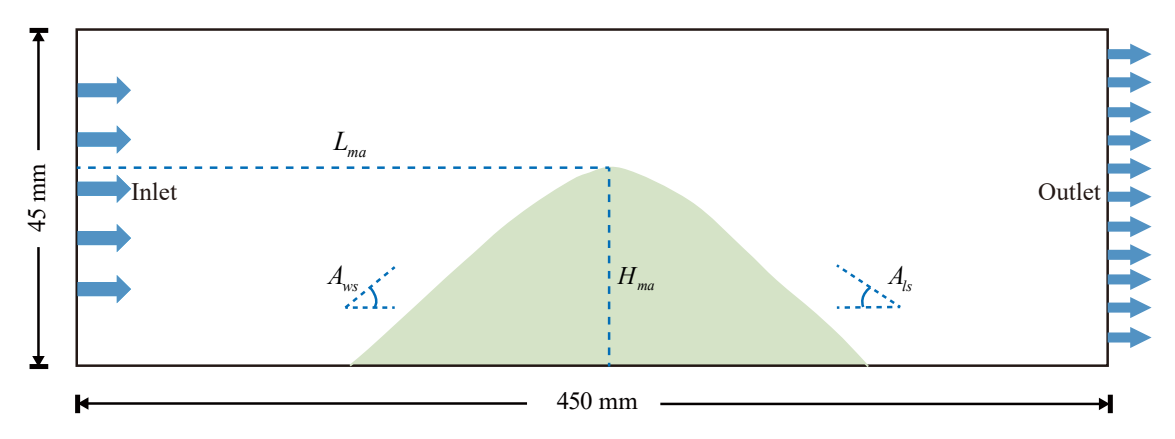


Fig. 3. Diagram illustrating the secondary fracture and dune parameters.

Table 2. Physical vs. numerical simulation results.

Parameters	$L_{ma}$ (m)	$H_{ma}$ (m)	$A_{ws}$ (°)	<i>A</i> <sub>ls</sub> (°)
Physical simulation	0.75	0.45	15	23
Numerical simulation	0.65	0.42	14	25
Relative error	13.33%	6.67%	6.67%	8.70%

#### 2.2 Box-Behnken experimental design

To investigate the influence of multiple parameters on the accumulation morphology of proppant in secondary fractures, a four-factor, four-level experimental framework was established based on the Box-Behnken design.  $H_{ma}$ ,  $A_{ws}$ ,  $A_{ls}$ , and  $L_{ma}$  were selected as response metrics (Fig. 3). Subsequently, a quadratic polynomial regression model was utilized to establish the correlation between each response variable and the four independent variables:

$$Y = \beta_0 + \sum_{i=1}^k \beta_i X_i + \sum_{i=1}^k \beta_{ii} X_i^2 + \sum_{i=1}^k \sum_{j=1}^k \beta_{ij} X_i X_j + e_0$$
 (12)

where Y represents the predicted response variable;  $\beta_0$ ,  $\beta_i$ ,  $\beta_{ij}$  and  $\beta_{ii}$  represent the regression coefficients for the constant term, linear term, interaction term, and quadratic term, respectively; X represents the coded values of the independent variable; k represents the number of independent variables; and  $e_0$  represents the model error.

Using regression analysis, the coefficients of the quadratic polynomial model were obtained to quantify the relationships among the studied variables. The validity and reliability of the model were assessed based on goodness-of-fit statistics and ANOVA. Data from 28 experiments were processed and analyzed using the Design-Expert software package.

#### 2.3 Simulation model verification

To validate the numerical model, a series of controlled physical simulation experiments were carried out under laboratory conditions. The experimental setup comprised a pumping system, an electronic control system, a sand-mixing tank system, a fracture-visualization system, an imaging system, a monitoring system, and a recovery system. The pumping system included a screw pump and high-pressure pipelines, and the control system coordinated the operation of the auxiliary subsystem. The sand-mixing system combined the proppant with the sand-carrying fluid at a specified ratio and ensured uniform dispersion through continuous stirring. The fracture-visualization cell included two parallel transparent glass plates, each 2.7 m long and 0.9 m high, with an aperture of 1.4 mm. The monitoring system incorporated an electromagnetic flowmeter with a measurement range of 0-2,000 L/min and an accuracy of  $\pm 0.5\%$ . The imaging module used a high-resolution camera to capture the temporal evolution of dune height throughout the whole experiment.

The proppant was mixed with the sand-carrying fluid at a specified ratio in the mixing tank and subsequently injected through ten inlet ports, each with a diameter of 1.4 mm, at an injection rate of 6 m<sup>3</sup>/h. The proppant used in the experiments consisted of quartz sand with particle-size ranges of 20/40, 40/70, and 70/140 mesh and a density of 2.500 kg/m<sup>3</sup>. The injection concentration of the proppant was maintained at 7%. The carrier fluid exhibited a viscosity of 1 mPa·s, as summarized in Table 1. Before each experiment, the fracture system was prefilled with the carrier fluid to eliminate air entrapment and ensure stable initial conditions. The proppant and fluid prepared in the mixing tank was continuously agitated and injected into the fracture through the inlet ports, while the whole process was continuously monitored and recorded by means of a high-resolution camera. The parameters employed in the numerical simulations were identical to those in the physical experiments, ensuring the consistency of the methodology and the comparability of results.

A comparison between dune morphology obtained from the physical experiments and numerical simulations is shown in Fig. 4, and the corresponding experimental data was summarized in Table 2. These simulations accurately reproduce the experimental dune morphologies, resulting in similar dune heights and lengths, with only a slight change in slope. Overall, the CFD-DEM simulation results are in good agreement with the experimental observation results, thus confirming the robustness and reliability of the numerical model.

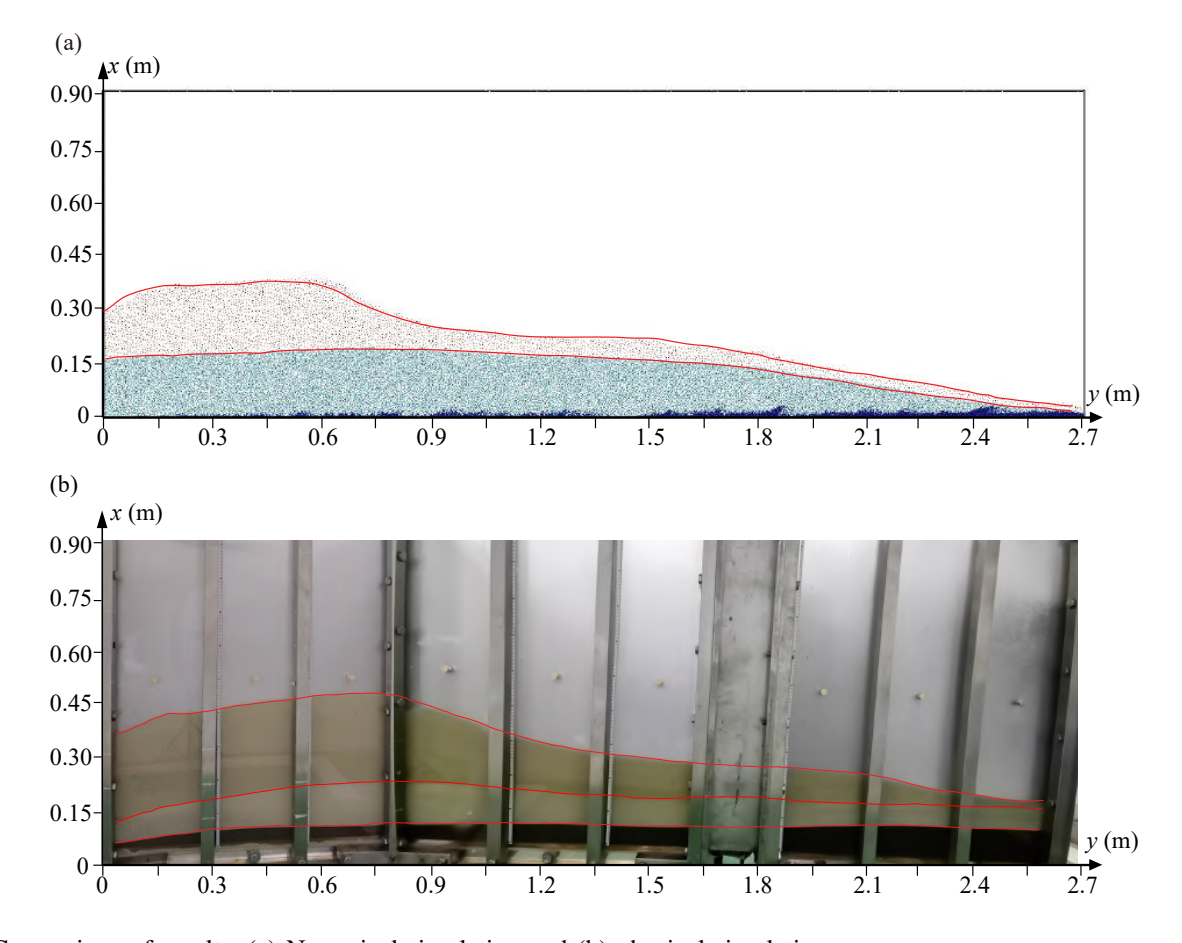


Fig. 4. Comparison of results: (a) Numerical simulation and (b) physical simulation.

#### 3. Results and discussion

#### 3.1 Effect of operational parameters

#### 3.1.1 Injection rate

The established model was employed to simulate proppant transport at injection rates of 0.005, 0.006, 0.008, 0.009, 0.010, 0.011, and 0.012 L/s. The proppant size was set to 0.6 mm (25-30 mesh), the density was 2,500 kg/m³, the viscosity of the sand-carrying fluid was 1.00 mPa·s, and the sand ratio was 14%. Each simulation was run for 15 s. The resulting proppant placement patterns under the seven injection rates are illustrated in Fig. 5.

According to the experimental results, a first-order kinetic equation was used to fit the data for parameters including  $H_{ma}$ ,  $L_{ma}$ ,  $A_{ws}$  and  $A_{ls}$ . The results are depicted in Fig. 6. The quantitative relationship between injection rate and dune parameters can be described by:

$$y = A_2 + \frac{A_1 - A_2}{1 + e^{(x - x_0)/dx}}$$
 (13)

where  $A_1$ ,  $A_2$ ,  $x_0$ , and dx are all constants. The fitting curves show a high degree of consistency with the experimental data, which effectively captures the development trends of proppant accumulation (Figs. 6(a)). With the injection rate increasing,  $L_{ma}$  increases gradually, whereas  $H_{ma}$  decreases gradually. At first, the reduction rate of  $H_{ma}$  is accelerated but then it slows

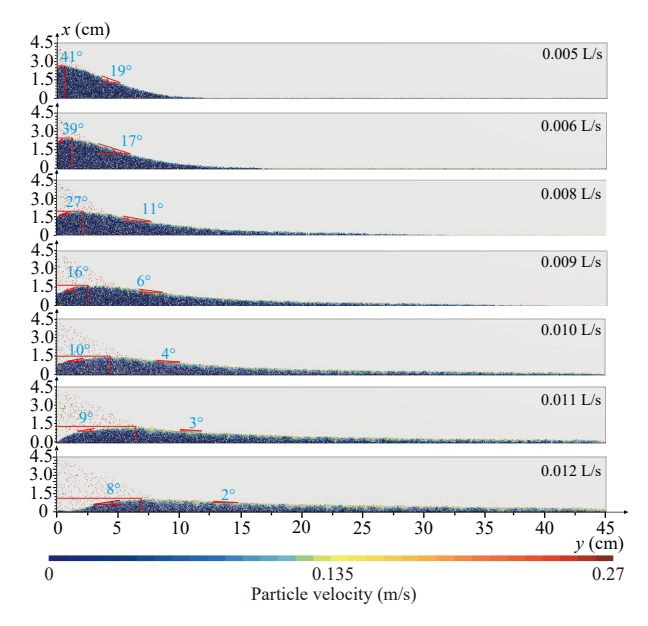


**Fig. 5**. Results of experiments conducted at various injection rates.

down as the injection rate continues to increase. For example, when the flow rate increases from 0.005 to 0.012 L/s,  $L_{ma}$  rises from 0.7 to 7 cm, which constitutes a significant increase of 900%. Meanwhile,  $H_{ma}$  decreases from 2.6 to 1.15 cm, with a reduction of about 55.8%.

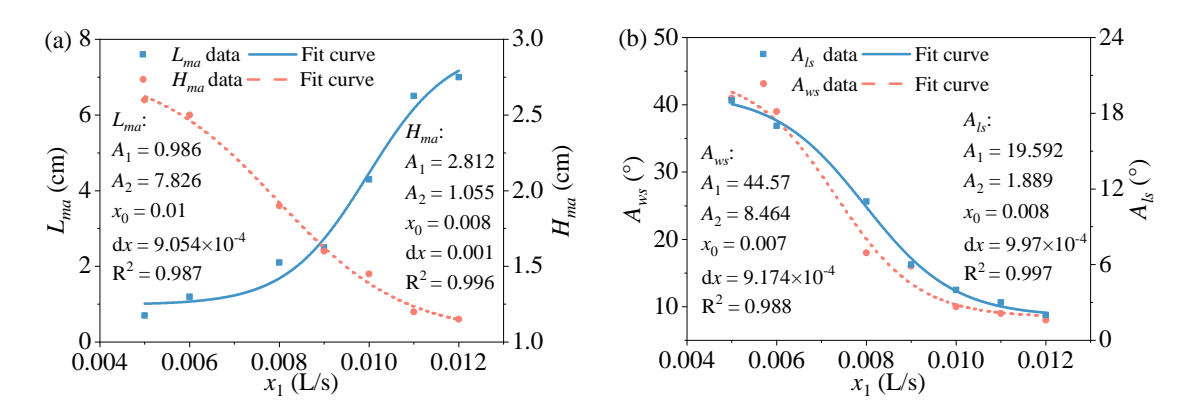


Fig. 6. Fitted curves of dune parameters at various injection rates: (a)  $L_{ma}$  and  $H_{ma}$  and (b)  $A_{ls}$  and  $A_{ws}$ .

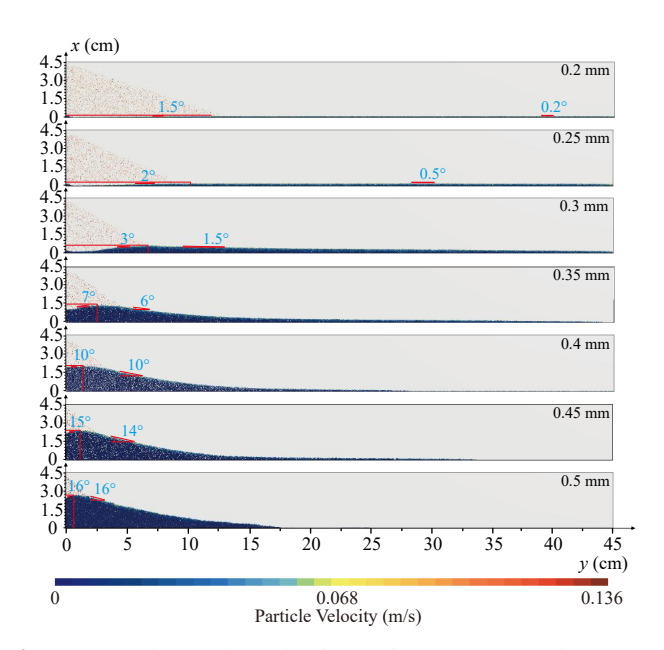


Fig. 7. Experimental results for various proppant sizes.

The observed trend can be attributed to the change of fluid and proppant flow dynamics under different injection rates. At low injection rates, the flow velocities of both the fluid and the proppant are relatively small, which leads to the limited carrying capacity of the fluid. Consequently, most of the proppant accumulates near the inlet region, forming high sand dunes in this region. As the injection rate increases, both the flow velocity and the proppant-carrying capacity of the fluid are improved, thus resulting in a longer transport distance and an increase in  $L_{ma}$ . Moreover, the higher injection rate enhances the diffusion and spreading of the proppant along the bottom of the fracture base, thus broadening the deposition area. Thirdly, increased injection rates raise the collision momentum between newly injected and previously deposited proppant particles, which drives the deposited proppant further downstream, and thereby reducing the overall dune height. However, when the injection rate becomes excessively high, the intensified fluid resistance acting on the proppant limits further increases in both  $L_{ma}$  and  $H_{ma}$ , thus leading to a gradual

stabilization of these parameters.

As the injection rate increases from 0.005 to 0.012 L/s,  $A_{ws}$  decreases from 41 to 8°, with a decrease of 80.5%, while  $A_{ls}$  decreases from 19 to 2°, with a decrease of 89.5% (Figs. 6(b)). The rates of decline in both angles accelerate at first, and then gradually slow down with the injection rate further increasing. This trend appears because a higher injection rate enhances the proppant-carrying capacity and diffusion effect of the fluid, and weakens the interparticle interactions among the proppant grains. Therefore, the deposition area of the proppant becomes expanded. Moreover, along with the increasing of injection rate, the erosive effect of fluid on the sand dunes becomes more pronounced, thus leading to rapid reductions in both  $A_{ws}$  and  $A_{ls}$ .

#### 3.1.2 Proppant size

Seven sets of experiments were conducted using proppant with diameters of 0.2 mm (70-80 mesh), 0.25 mm (60-70 mesh), 0.3 mm (50-60 mesh), 0.35 mm (45-50 mesh), 0.4 mm (40-45 mesh), 0.45 mm (35-40 mesh), and 0.5 mm (30-35 mesh). The established model was employed to perform the corresponding simulations under a flow rate of 0.04 L/s. The proppant concentration was maintained at 14%, the proppant density was 2,500 kg/m³, and the viscosity of sand-carrying fluid was 1.00 mPa·s. Each simulation was run for 15 s. The resulting proppant placement patterns for the seven particle sizes were illustrated in Fig. 7.

Based on the experimental results, a first-order kinetic equation was employed to analyze the data for parameters, including  $H_{ma}$ ,  $L_{ma}$ ,  $A_{ws}$ , and  $A_{ls}$  (Fig. 8). The dependence of the dune parameters on proppant size can be expressed as:

$$y = A_2 + \frac{A_1 - A_2}{1 + e^{(x - x_0)/dx}}$$
 (14)

where  $A_1$ ,  $A_2$ ,  $x_0$ , and dx are constants. The fitted curves show a high level of consistency with the experimental data, effectively capturing the evolving trends in the proppant placement process. As shown in Fig. 8(a), with increasing proppant particle size,  $L_{ma}$  gradually decreases, while  $H_{ma}$  increases. The slope of the curves initially rises but then gradually declines. For instance, as the proppant size increases from 0.2

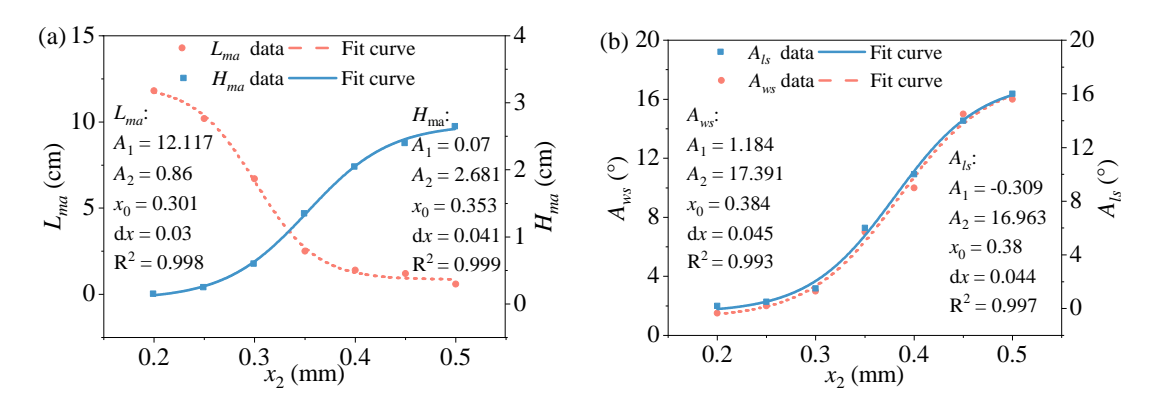


Fig. 8. Fitted curves of dune parameters at various propant sizes: (a)  $L_{ma}$  and  $H_{ma}$ , and (b)  $A_{ls}$  and  $A_{ws}$ .

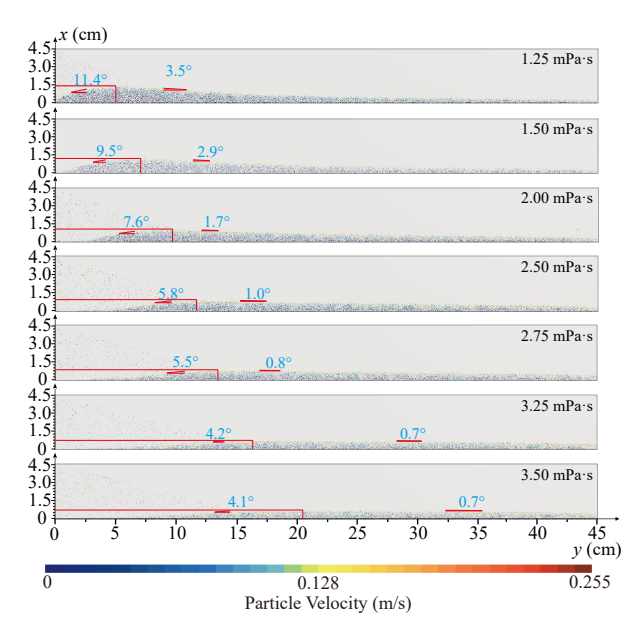


Fig. 9. Results of experiments at various sand-carrying fluid viscosities.

to 0.5 mm,  $H_{ma}$  increases by approximately 1,667% (from 0.15 to 2.65 cm), while  $L_{ma}$  decreases by about 94.9% (from 11.8 to 0.6 cm).

The main reason for these trends is that, at the same density, larger proppant particles possess greater mass and surface area. As a result, they are subjected to stronger gravitational and drag forces during transport, which reduce their transport distance while promote greater accumulation, thus increasing the value of  $H_{ma}$ .

As the particle size of proppant increases, both  $A_{ws}$  and  $A_{ls}$  increase, although the rate of increase begins to accelerate and then gradually decreases. Specifically,  $A_{ws}$  increases from 1.5 to 16°, representing a rise of approximately 967%, while  $A_{ls}$  increases from 0.2 to 16°, corresponding to an increase of about 7,900% (Figs. 8(b)). This phenomenon is mainly due to the fact that smaller proppant particles are transported for longer distances, covering a wider area and exhibiting a slower rate of dune height growth, which results in relatively flat dunes with smaller  $A_{ws}$  and  $A_{ls}$ . As the proppant size increases,

gravitational effects enhance particle settling, leading to more rapid dune height development. Larger particles also generate greater interparticle spacing during accumulation, thereby increasing both  $A_{ws}$  and  $A_{ls}$ . However, once the particle size exceeds a certain threshold, the growth rate of dune height slows down, and particle slippage becomes more pronounced during deposition. This behavior promotes a broader deposition zone and leads to the stabilization of  $A_{ws}$  and  $A_{ls}$ .

#### 3.1.3 Sand-carrying fluid viscosity

The sand-carrying fluids with viscosities of 1.25, 1.50, 2.00, 2.50, 2.75, 3.25, and 3.50 mPa·s were set for the numerical simulations. The proppant size was set to 0.6 mm (25-30 mesh), the density was 2,500 kg/m³, and the sand ratio was 14%. The injection rate was maintained at 0.01 L/s, and each simulation was run for 15 s. The proppant placement patterns obtained under seven fluid viscosities are illustrated in Fig. 9.

Based on the experimental results, a first-order kinetic equation was employed to analyze the variations in  $H_{ma}$ ,  $L_{ma}$ ,  $A_{ws}$ , and  $A_{ls}$ . The corresponding results are illustrated in Fig. 10. The quantitative relationship between proppant size and the deposition parameters can be expressed as:

$$y = A_1 e^{-x/t_1} + y_0 (15)$$

 $L_{ma}$  increases progressively with increasing fluid viscosity, and the rate of increase becomes more pronounced at higher viscosities. On the contrary,  $H_{ma}$  decreases as viscosity increases, but the decrease rate gradually slows down, as illustrated in Fig. 10(a). When the viscosity increases from 1.25 to 3.50 mPa·s,  $L_{ma}$  increases from 5.0 to 20.5 cm, representing an increase of approximately 310%, while  $H_{ma}$  decreases from 1.4 to 0.72 cm, corresponding to a reduction of about 49%. This behavior is primarily attributed to the enhanced proppantcarrying capacity of the fluid as viscosity rises, which allows proppant to be transported farther position into the fractures, thus expanding the deposition area but reducing the dune height. Furthermore, higher viscosity increases the drag force acting on the proppant, prolonging its suspension time and promoting a more uniform distribution of particles within the fracture network.

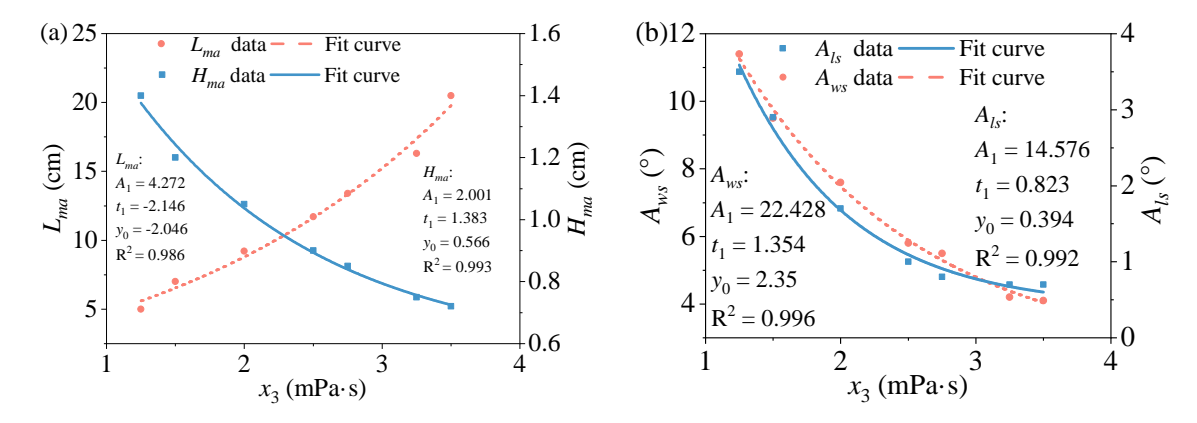
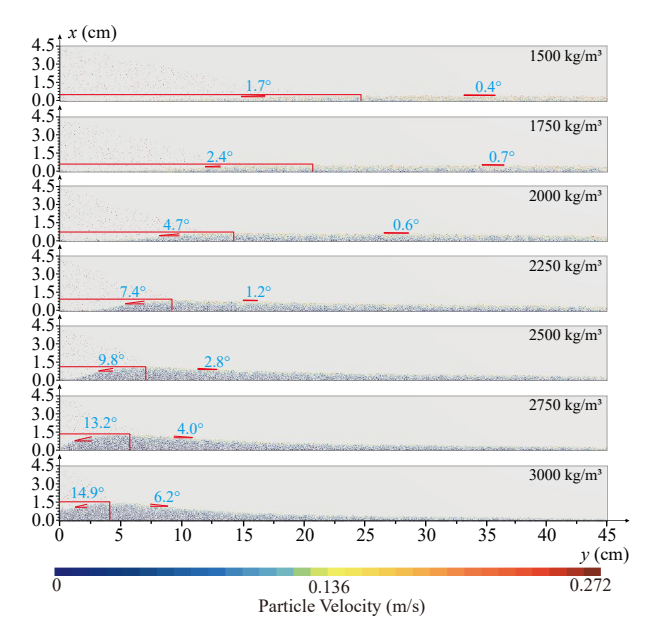


Fig. 10. Fitted curves of dune parameters at various sand-carrying fluid viscosities: (a)  $L_{ma}$  and  $H_{ma}$ , and (b)  $A_{ls}$  and  $A_{ws}$ .



**Fig. 11**. Results of experiments at various proppant densities.

With increasing fluid viscosity,  $A_{ws}$  of the dune gradually decreases, although the rate of decrease is slower. Specifically, when the viscosity increases from 1.25 to 3.50 mPa·s,  $A_{ws}$  decreases from 11.4° to 4.1°, indicating a reduction degree of about 64%, while  $A_{ls}$  decreases from 3.5° to 0.7°, corresponding to a reduction degree of about 80%, as shown in Fig. 10(b). This behavior can be attributed to the longer residence time of proppant particles within the fluid at higher viscosities, which promotes a broader deposition area and reduces both  $A_{ws}$  and  $A_{ls}$ . In addition, higher viscosity diminishes the inter particle collisions and kinetic energy exchange during transport, resulting in a more uniform proppant distribution and a flatter dune shape.

During the process of sand dune formation, an initial basal layer is first established at the bottom of the fracture, and then it is locally accumulated in specific regions. With the fluid viscosity increasing, the height of this basal layer gradually rises, and its areal coverage expands accordingly. However, the existence of coarser particles can lead to the formation

of larger unfilled zones within the fracture, which might have an adverse impact on methane flow and eventually reduce the production efficiency of coalbed methane.

#### 3.1.4 Proppant density

Simulations were carried out using proppant with densities of 1,500, 1,750, 2,000, 2,250, 2,500, 2,750, and 3,000 kg/m³, respectively. The proppant size was fixed at 0.6 mm (25-30 mesh), with a sand-carrying fluid viscosity of 1.00 mPa·s and a sand ratio of 14%. The injection rate was maintained at 0.012 L/s, and each simulation was run for 8 s. The resulting proppant placement patterns obtained under seven proppant densities are illustrated in Fig. 11.

According to the experimental results, the  $H_{ma}$ ,  $L_{ma}$ ,  $A_{ws}$ , and  $A_{ls}$  were fitted using a first-order kinetic equation (Fig. 12). The quantitative relationships between proppant density and the dune parameters can be expressed as follows:

$$y = A_1 e^{-x/t_1} + y_0 (16)$$

 $L_{ma}$  decreases progressively with increasing proppant density, while  $H_{ma}$  increases. Specifically, as the proppant density rises from 1,500 to 3,000 kg/m<sup>3</sup>,  $L_{ma}$  decreases from 24.6 to 4.1 cm, an 83.3% reduction, while the height increases from 0.5 to 1.52 cm, reflecting a 204% increase, as illustrated in Fig. 12(a). These results indicate that increasing the proppant density enhances the gravitational force acting on the particles, while the fluid drag remains almost unchanged, resulting in a faster sedimentation rate. Consequently, both the transport distance and accumulation range decrease, thus leading to a reduction in  $L_{ma}$  and a corresponding increase in  $H_{ma}$ . As depicted in Fig. 12(b), both  $A_{ws}$  and  $A_{ls}$  increase with rising proppant density. Specifically, when the proppant density increases from 1,500 to 3,000 kg/m<sup>3</sup>,  $A_{ws}$  rises from 1.7° to 14.9°, marking an increase of 776.5%. Similarly,  $A_{ls}$  rises from 0.4° to 6.2°, reflecting a 145% increase. This behavior is mainly due to the higher settling velocity of particles with higher density in the fracture, which promotes faster accumulation and steeper dune slopes. In addition, the greater proppant density enhances the contact and filling efficiency among particles during the deposition process, thus further contributing to the increase in

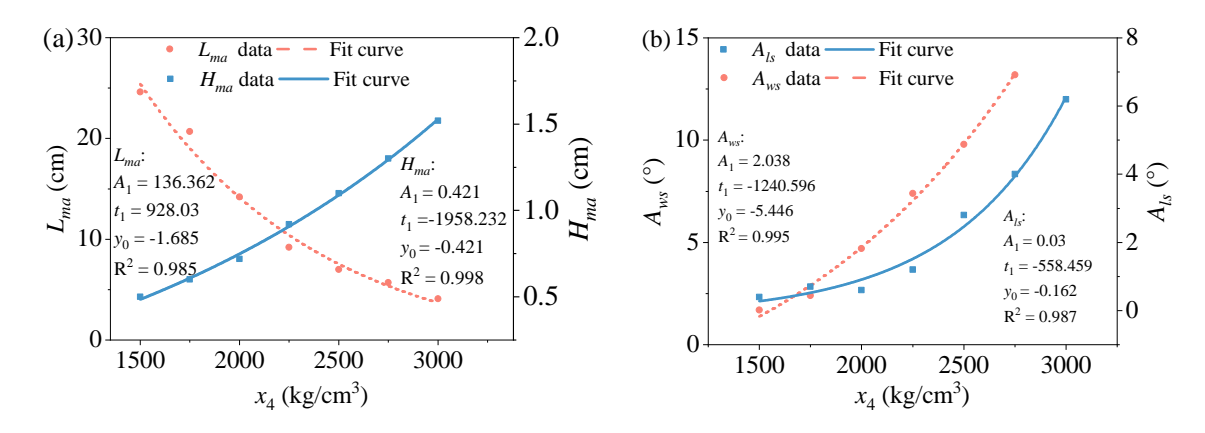


Fig. 12. Fitted curves of dune shape parameters at various proppant densities: (a)  $L_{ma}$  and  $H_{ma}$ , and (b)  $A_{ls}$  and  $A_{ws}$ .

Monitoring value Response index No.  $A_{ls}$  (°)  $x_1$  (L/s)  $x_3$  (mPa·s)  $x_4$  (kg/m<sup>3</sup>)  $A_{ws}$  (°)  $x_2$  (mm)  $H_{ma}$  (cm)  $L_{ma}$  (cm) 1 0.005 0.6 1.00 2,500 2.6 0.7 41 19 2 0.04 0.2 1.00 41 1.5 2,500 0.15 0.2 0.6 5 3 0.01 1.25 2,500 1.4 11.4 3.5 4 0.012 1.00 1,500 0.5 24.6 1.7 0.4 0.6 5 39 0.006 0.6 1.00 2,500 2.5 1.2 17 0.04 0.25 0.25 0.5 6 1.00 2,500 40.5 2 7 7 0.01 0.6 1.5 2,500 1.2 9.5 2.9 8 0.012 1.00 1,750 0.6 20.7 0.7 0.6 2.4 9 0.008 2,500 1.9 18 0.6 1.00 2.1 11 10 0.04 2,500 0.6 15 1.5 0.3 1.00 3 11 0.01 0.6 2 2,500 1.05 9.2 7.6 1.7 12 0.012 0.6 1.00 2,000 0.72 14.2 4.7 0.6 13 0.009 0.6 1.00 2,500 1.6 2.5 16 6 0.04 14 0.35 1.00 2,500 1.35 15 7 6 15 0.01 0.6 2.5 2,500 0.9 11.7 5.8 1 16 0.012 0.6 1.00 2,250 0.92 9.2 7.4 1.2 17 0.01 0.6 1.00 2,500 1.3 5.3 12 4.2

Table 3. Experimental design and results.

 $A_{ws}$  and  $A_{ls}$ .

## 3.2 Response surface analysis of experimental results

To support hydraulic fracturing operations to the greatest extent and evaluate related indicators effectively after completion, based on the data in Table 3, a multiple regression analysis was carried out by using Design-Expert. This analysis led to the development of equations describing the relationships between each response variable and the related parameters:

$$H_{ma}(x) = 51.097x_1 + 7.156x_2 - 0.339x_3 + 0.001x_4 - 5.701$$
(17)

$$L_{ma}(x) = -87.088x_1 - 80.795x_2 + 4.814x_3$$
$$-0.017x_4 + 92.818$$
 (18)

$$A_{ws}(x) = -160.774x_1 + 19.136x_2 - 5.43x_3 + 0.014x_4 - 23.856$$
(19)

$$A_{ls}(x) = 296.870x_1 + 37.308x_2 - 2.784x_3 + 0.007x_4 - 33.436$$
 (20)

where  $x_1$  represents the injection rate;  $x_2$  represents the proppant size;  $x_3$  represents the sand-carrying fluid viscosity; and  $x_4$  represents the proppant density.

The p value for the regression model of  $H_{ma}$  is 0.0009, indicating the strong statistical significance of the model. Moreover, the p value for the lack of fit exceeds 0.05, confirming that the regression equation accurately represents the relationship between  $H_{ma}$  and the influencing parameters. In addition, the p values of proppant size, sand-carrying fluid viscosity, injection rate, and proppant density were 0.0065, 0.0008, 0.0177, and 0.0059, respectively. All of which are statistically significant. Among these, the injection rate and sand-carrying fluid viscosity exhibit a positive correlation with dune accumulation height. The relative importance of the factors affecting  $H_{ma}$  can be ranked as follows: Proppant size p proppant density p injection rate p sand-carrying fluid viscosity.

The p value for  $L_{ma}$  regression model is less than 0.0001, indicating that the model is statistically significant. The fitted regression equation accurately represents the relationship between the horizontal distance and the parameters. In addition, the p values of proppant size, sand-carrying fluid viscosity, injection rate, and proppant density are 0.602, 0.0001, 0.001, and less than 0.001, respectively. Specifically, proppant size, sand-carrying fluid viscosity, and proppant density are statistically significant predictors, whereas injection rate is not statistically significant. The regression analysis shows that both the sand-carrying fluid viscosity and the injection rate exhibit a positive correlation with  $L_{ma}$ , while proppant size and proppant density are negatively correlated with this parameter. The relative importance of the factors affecting  $L_{ma}$  can be ranked as follows: Proppant density > proppant size > sandcarrying fluid viscosity.

The p value for  $A_{ws}$  regression model is 0.0261, indicating that the model is statistically significant. The lack-of-fit p exceeds 0.05, suggesting no significant lack of fit; thus, the fitted regression equation adequately represents the relationship between  $A_{ws}$  and the parameters. The p values of proppant size, sand-carrying fluid viscosity, injection rate, and proppant density are 0.5676, 0.5297, 0.0192, and 0.0251, respectively. Among these, sand-carrying fluid viscosity and proppant density are statistically significant predictors, whereas inlet rate and proppant size are not. The regression coefficients indicate that proppant size and proppant density are positively correlated with  $A_{ws}$ , whereas inlet rate and sand-carrying fluid viscosity are negatively correlated with  $A_{ws}$ . The relative importance of the factors affecting  $A_{ws}$  can be ranked as follows: Sand-carrying fluid viscosity > proppant density.

The p value for  $A_{ls}$  regression model is 0.0434, indicating that the model is statistically significant. The lack-of-fit p exceeds 0.05, suggesting no significant lack of fit; therefore, the fitted regression equation adequately represents the relationship between  $A_{ls}$  and the parameters. The p values of proppant size, sand-carrying fluid viscosity, injection rate, and proppant density are 0.0876, 0.0496, 0.0423, and 0.0635, respectively. Among these, proppant size and sand-carrying fluid viscosity are statistically significant, whereas inlet rate and proppant density are not. The regression coefficients reveal

that proppant size and proppant density are positively correlated with  $A_{ls}$ , whereas injection rate and sand-carrying fluid viscosity are negatively correlated. The relative importance of factors affecting  $A_{ls}$  can be ranked as follows: Sand-carrying fluid viscosity > proppant size.

## 3.3 Optimization of proppant injection parameters

In practical applications, it is essential to form largescale, long-distance proppant accumulation within the hydrofracture. This objective requires maximizing  $H_{ma}$  and  $L_{ma}$ while minimizing both  $A_{ws}$  and  $A_{ls}$ . By solving the regression equations, the optimal parameter combinations under the experimental conditions can be determined. When the injection rate is 0.04 L/s, proppant size is 0.6 mm, fluid viscosity is 1.00 mPa·s, and proppant density is 3,000 kg/m<sup>3</sup>, the  $H_{ma}$ reaches a maximum of 3.588 cm, accounting for 79.7% of the hydro-fracture height. When the injection rate is 0.005 L/s, proppant size is 0.2 mm, sand-carrying fluid viscosity is 3.5 mPa·s, and proppant density is 1,500 kg/m<sup>3</sup>,  $L_{ma}$  is maximized at 67.508 cm. When the injection rate is 0.012 L/s, proppant size is 0.557 mm, sand-carrying fluid viscosity is 1.274 mPa·s, and proppant density is 1,585.745 kg/m<sup>3</sup>, the minimum  $A_{ws}$ is 0.047°. Additionally, when the injection rate is 0.007 L/s, proppant size is 0.533 mm, sand-carrying fluid viscosity is 1.518 mPa·s, and proppant density is 2,338.419 kg/m<sup>3</sup>, the minimum  $A_{ls}$  is  $0.101^{\circ}$ .

In field fracturing operations, fracture size parameters can be obtained from test wells. Based on the relationships among injection rate, proppant size, sand-carrying fluid viscosity, proppant density, and dune parameters described in this paper, the injection parameters of the proppant can be determined to ensure long-distance proppant placement.

#### 4. Conclusions

To investigate the transport and placement behavior of proppant within secondary fractures, this study presented a CFD-DEM simulation model. Corresponding multiple linear regression equations were established, the influences of key factors on the response variables were quantified, and the optimal parameter combinations under various conditions were determined. The main findings are as follows:

- 1) Proppant particles initially spread evenly at the bottom of a part of the fracture, forming an initial deposition layer with a limited height. As the injection continues, a dune begins to develop at a local location. With the progressively increasing dune height, the growing structure partially hinders the inflow of extra proppant. Subsequently, a portion of particles accumulate on the windward side of the dune, while others collide with particles near the top of the dune and are deposited on the leeward side. This dynamic process results in a continuous increase in both the dune height and its areal extent.
- An increase in injection rate enhances the formation of fluid turbulence and vertex, thus intensifying the particle-particle interactions. Because of the higher rel-

ative particle velocity, this effect also increases the drag force acting on the proppant. Proppant size affects the transport and placement behaviors by changing particle mass and surface area: Larger particles possess greater mass and surface area than smaller ones, which leads to stronger gravitational and drag forces during transport, thus making them more likely to settle near the inlet. Variations in the viscosity of the sand-carrying fluid directly affect its proppant-carrying capacity. The higher the viscosity, the longer suspension times and the longer transport distances. Similarly, alterations in the proppant density change the gravitational force acting on individual particles; as density increases, the transport distance decreases, promoting earlier deposition and accumulation near the inlet region.

- 3) The relative importance of factors influencing  $H_{ma}$  can be arranged as follows: Proppant size > proppant density > injection rate > sand-carrying fluid viscosity. For  $L_{ma}$ , the ranking is: Proppant density > proppant size > sand-carrying fluid viscosity. The factors affecting  $A_{ws}$  can be ordered by importance as sand-carrying fluid viscosity > proppant density, while those influencing the  $A_{ls}$  are ranked as sand-carrying fluid viscosity > proppant size.
- 4) Under the specified experimental conditions of 0.04 L/s injection rate, 0.6 mm proppant size, 1.00 mPa·s sand-carrying fluid viscosity, and 3,000 kg/m³ proppant density, the  $H_{ma}$  reaches 3.588 cm, accounting for 79.7% of the fracture height. Conversely, when the injection rate is reduced to 0.005 L/s, at the smaller proppant size of 0.2 mm, higher sand-carrying fluid viscosity of 3.5 mPa·s, and lower proppant density of 1,500 kg/m³,  $L_{ma}$  extends to the maximum value of 67.508 cm, corresponding to 15 times the fracture height.

However, apart from the four primary factors considered in this study, other potential influencing variables were not examined. Therefore, additional factors should be included in future research to further improve the accuracy and robustness of the prediction model.

#### Acknowledgements

This work was supported by the Guizhou Provincial Key Technology R&D Program (No. QianKe-HeZhiCheng[2023]YiBan369), the Guizhou Geological Exploration Fund Project (No. 52000024P0048BH101732), the Fundamental Research Funds for the Central Universities (No. 2023CDJKYJH071) and the Guizhou Province Science and Technology Innovation Talent Team (No. Qian Ke He Platform Talent-CXTD[2023]013).

#### **Conflict of interest**

The authors declare no competing interest.

**Open Access** This article is distributed under the terms and conditions of the Creative Commons Attribution (CC BY-NC-ND) license, which permits unrestricted use, distribution, and reproduction in any medium, provided the original work is properly cited.

#### References

- Akhshik, S., Rajabi, M. Simulation of proppant transport at intersection of hydraulic fracture and natural fracture of wellbores using CFD-DEM. Particuology, 2022, 63: 112-124.
- Alvandifar, N., Mahravan, E., Christensen, K. G., et al. Modeling of two-phase CO<sub>2</sub> ejectors using an Eulerian-Eulerian two-fluid approach. International Journal of Refrigeration, 2025, 177: 338-350.
- Anjum, J., Salma, A., Hanumagowda, B. N., et al. Squeeze film lubrication between two different spheres: MHD-couple stress fluid model. International Communications in Heat and Mass Transfer, 2025, 166: 109133.
- Basiuk, L., Irou Roschzttardtz, F., Fernandez, M. E., et al. Proppant transport in scaled experiments: Effect of drainage configuration and fracture wall roughness. Journal of Petroleum Science and Engineering, 2022, 208: 109433.
- Cheng, Q., Li, H., Huang, B., et al. Migration and distribution characteristics of proppant at the corner of horizontal fracture network in coal seam. Frontiers in Earth Science, 2021, 9: 792232.
- Cundall, P. A., Strack, O. D. L. A discrete numerical model for granular assemblies. Geotechnique, 1979, 29(1): 47-65.
- Difelice, R. The voidage function for fluid particle interaction systems. International Journal of Multiphase Flow, 1994, 20(1): 153-159.
- Eltom, H. Modeling and simulating biogenically-controlled permeability in gas reservoirs. Marine and Petroleum Geology, 2024, 167: 106951.
- Gislason, K., Fredsoe, J., Sumer, B. M. Flow under standing waves part 2. Scour and deposition in front of breakwaters. Coastal Engineering, 2009, 56(3): 363-370.
- Heriawan, M. N., Koike, K. Coal quality related to microfractures identified by CT image analysis. International Journal of Coal Geology, 2015, 140: 97-110.
- Hosseini, N., Khoei, A. R. Numerical simulation of proppant transport and tip screen-out in hydraulic fracturing with the extended finite element method. International Journal of Rock Mechanics and Mining Sciences, 2020, 128: 104247.
- Hou, L., Cheng, Y., Wang, X., et al. Effect of slickwateralternate-slurry injection on proppant transport at field scales: A hybrid approach combining experiments and deep learning. Energy, 2022, 242: 122987.
- Kern, L. R., Perkins, T. K., Wyant, R. E. The mechanics of sand movement in fracturing. Transactions of the American Institute of Mining and Metallurgical Engineers, 1959, 216: 403-405.
- Kray, T., Franke, J., Frank, W. Magnus effect on a rotating soccer ball at high Reynolds numbers. Journal of Wind Engineering and Industrial Aerodynamics, 2014, 124: 46-53.
- Li, H., Huang, B., Han, X., et al. Pulse effects on propapnt transport and dune shape in vertical fracture applied in coalbed methane mining engineering during the pulse hydraulic fracturing. Geoenergy Science and Engineering,

- 2023, 229: 212128.
- Li, H., Hu, Q., Zhu, R., et al. Reactive transport modeling of water-CO<sub>2</sub>-rock interactions in clay-coated sandstones and implications for CO<sub>2</sub> storage. Advances in Geo-Energy Research, 2025, 17(2): 121-134.
- Li, J., Han, X., He, S., et al. Effect of proppant sizes and injection modes on proppant transportation and distribution in the tortuous fracture model. Particuology, 2024, 84: 261-280.
- Li, R., Wang, S., Lyu, S., et al. Geometry and filling features of hydraulic fractures in coalbed methane reservoirs based on subsurface observations. Rock Mechanics and Rock Engineering, 2020, 53(5): 2485-2492.
- Liao, Q., Wang, B., Chen, X., et al. Reservoir stimulation for unconventional oil and gas resources: Recent advances and future perspectives. Advances in Geo-Energy Research, 2024, 13(1): 7-9.
- Lu, Y., Zhao, G., Ge, Z., et al. Challenges and development direction of deep fragmented soft coalbed methane in china. Earth Energy Science, 2025, 1(1): 38-64.
- Lv, M., Guo, T., Chen, M., et al. Study on proppant flowback mechanism during post-fracturing stage based on CFD-DEM. Earth Energy Science, 2025, 1(3): 256-269.
- Ma, W., Perng, J., Tomac, I. Experimental investigation of proppant flow and transport dynamics through fracture intersections. Geomechanics for Energy and the Environment, 2022, 30: 100232.
- Mei, R. An approximate expression for the shear lift force on a spherical-particle at finite reynolds-number. International Journal of Multiphase Flow, 1992, 18(1): 145-147.
- Mirjalily, S. A. A. Calibration of the k- $\omega$  shear stress transport turbulence model for shock wave boundary layer interaction in a sern using machine learning. Engineering Analysis with Boundary Elements, 2023, 146: 96-104.
- Mohapatra, S. C., Soares, C. G. Boussinesq model for two-fluid system with surface- and interfacial tension. Applied Ocean Research, 2024, 152: 104183.
- Mou, P., Pan, J., Wang, K., et al. Influences of hydraulic fracturing on microfractures of high-rank coal under different in-situ stress conditions. Fuel, 2021, 287: 119566.
- Patel, S., Wilson, I., Sreenivasan, H., et al. Numerical simulations of proppant transportation in cryogenic fluids: Implications on liquid helium and liquid nitrogen fracturing for subsurface hydrogen storage. International Journal of Hydrogen Energy, 2024, 56: 924-936.
- Richesson, S., Sahimi, M. Hertz-Mindlin theory of contacting grains and the effective-medium approximation for the permeability of deforming porous media. Geophysical Research Letters, 2019, 46(14): 8039-8045.
- Rivas, E., Gracie, R. A monolithic coupled hydraulic fracture model with proppant transport. Computer Methods in Applied Mechanics and Engineering, 2020, 372: 113361.
- Shamshirband, S., Malvandi, A., Karimipour, A., et al. Performance investigation of micro- and nano-sized particle erosion in a 90° elbow using an anfis model. Powder Technology, 2015, 284: 336-343.
- Shiozawa, S., McClure, M. Simulation of proppant transport

- with gravitational settling and fracture closure in a threedimensional hydraulic fracturing simulator. Journal of Petroleum Science and Engineering, 2016, 138: 298-314.
- Suri, Y., Islam, S. Z., Hossain, M. A new CFD approach for proppant transport in unconventional hydraulic fractures. Journal of Natural Gas Science and Engineering, 2019, 70: 102951.
- Suri, Y., Islam, S. Z., Hossain, M. Effect of fracture roughness on the hydrodynamics of proppant transport in hydraulic fractures. Journal of Natural Gas Science and Engineering, 2020, 80: 103401.
- Wang, F., Xu, H., Wang, S., et al. Fluid flow and efficient development technologies in unconventional reservoirs: State-of-the-art methods and future perspectives. Advances in Geo-Energy Research, 2024, 12(3): 237-240.
- Wang, X., Yao, J., Gong, L., et al. Numerical simulations of proppant deposition and transport characteristics in hydraulic fractures and fracture networks. Journal of Petroleum Science and Engineering, 2019, 183: 106401.
- Wei, Z., Sheng, M., Li, J., et al. Pressure diagnostics in hydraulic fracturing for unconventional completion optimization. Advances in Geo-Energy Research, 2025, 17(3): 196-211.
- Wen, Q., Wang, S., Duan, X., et al. Experimental investigation of proppant settling in complex hydraulic-natural fracture system in shale reservoirs. Journal of Natural Gas Science and Engineering, 2016, 33: 70-80.
- Wood, D. A. Variable interaction empirical relationships and machine learning provide complementary insight to experimental horizontal wellbore cleaning results. Advances in Geo-Energy Research, 2023, 9(3): 172-184.
- Wu, M., Li, H., Wang, L., et al. μCT quantitative assessment of the pore-fracture structures and permeability behaviors of long-flame coal treated by infrared rapid heating. Energy, 2023, 274: 127308.
- Xiao, H., Li, Z., He, S., et al. Experimental study on propapant diversion transportation and multi-size propant distribution in complex fracture networks. Journal of Petroleum Science and Engineering, 2021, 196: 107800.
- Xu, F., Hou, W., Xiong, X., et al. The status and development strategy of coalbed methane industry in china. Petroleum Exploration and Development, 2023, 50(4): 765-783.
- Yamashiro, B. D., Tomac, I. A numerical study of neutrally buoyant slickwater proppant flow and transport in rough fractures. Geomechanics for Energy and the Environment, 2022, 29: 100266.
- Zheng, Y., Zhou, M. M., Kuru, E., et al. Proppant transport in rough fracture networks using supercritical CO<sub>2</sub>. Petroleum Science, 2024, 21(3): 1852-1864.
- Zhou, Z., Kuang, S., Chu, K., et al. Discrete particle simulation of particle-fluid flow: Model formulations and their applicability. Journal of Fluid Mechanics, 2010, 661: 482-510.
- Zhu, H., Zhou, Z., Yang, R., et al. Discrete particle simulation of particulate systems: A review of major applications and findings. Chemical Engineering Science, 2008, 63(23): 5728-5770.